Erschienen in: Soft Matter ; 17 (2021). - S. 6519-6535
https://dx.doi.org/10.1039/D1SM00635E

Phase behaviour in 2D assemblies of dumbbell-shaped colloids generated under geometrical confinement†

Rouven Stuckert,‡[a] Anton Lüders,‡[b] Alexander Wittemann*[a] and Peter Nielaba*[b]

The structure formation and the phase behaviour of monolayers of dumbbell-shaped colloids are explored. For this, we conduct Langmuir–Blodgett experiments at the air/water interface and conventional Brownian dynamic simulations without hydrodynamic interactions. Using Voronoi tessellations and the probability density of the corresponding shape factor of the Voronoi cells $p(\zeta)$, the influence of the area fraction ϕ on the structure of the monolayers is investigated. An increase of the area fraction leads to a higher percentage of domains containing particles with six nearest neighbours and a sharper progression of $p(\zeta)$. Especially in dense systems, these domains can consist of aligned particles with uniform Voronoi cells. Thus, the increase of ϕ enhances the order of the monolayers. Simulations show that a sufficient enhancement of ϕ also impacts the pair correlation function which develops a substructure in its first maxima. Furthermore, we find that reducing the barrier speed in the Langmuir–Blodgett experiments enhances the final area fraction for a given target surface pressure which, in turn, also increases the percentage of particles with six nearest neighbours and sharpens the progression of $p(\zeta)$. Overall, the experiments and simulations show a remarkable qualitative agreement which indicates a versatile way of characterising colloidal monolayers by Brownian dynamics simulations. This opens up perspectives for application to a broad range of nanoparticle-based thin film coatings and devices.

1 Introduction

The assembly of nanoparticles has sparked considerable interest as a subject with applications in the field of new materials with novel properties which manifest themselves, for example in remarkable optical[1,2] or magnetic[3] characteristics. Special attention has been paid to the assembly of anisotropic nanoparticles such as rods[4] and ellipsoids[5] as their assembly might induce direction-dependent properties which are, for example useful for sensing or filtering materials.

A powerful technique for the large-scale 2D assembly of particles at the air/water interface is the Langmuir–Blodgett method.[6] Here, movable barriers are utilised to compress particles to a high density two-dimensional film. A wide variety of particles, both organic and inorganic, have been used to create monolayers *via* this method. Diverse shapes such as plates,[7] rods[4] and ellipsoids[5] were used successfully.

Developments in the field of nanoparticle synthesis have made it possible to obtain dumbbell particles on the gram scale.[8] Dumbbell particles can be assembled into densely packed structures but are known only to crystallise under strong confinement such as an external electric field.[9–12] Several works have investigated the assembly of dumbbells into clusters,[13] 2D films[14,15] and 3D colloidal crystals.[9]

Computer simulations are an important tool to analyse the crystallisation and the order of complex colloidal systems and colloidal monolayers. A multitude of well established algorithms such as the Monte Carlo algorithms[16,17] and the Brownian dynamics algorithm[18,19] were utilised to study the behaviour of various kinds of particles reaching from simple hard spheres[20] or two-dimensional disks[21] to complex asymmetric shapes.[22] Recently, molecular dynamics simulations of two-dimensional layers of soft colloidal dumbbells indicated a rich variety of different structural arrangements of dumbbell-shaped particles in 2D.[23]

With the application of Brownian dynamics simulations, it was possible to show the significant impact of confinement on

[a] *Colloid Chemistry, Department of Chemistry, University of Konstanz, Universitaetsstrasse 10, D-78464 Konstanz, Germany. E-mail: alexander.wittemann@uni-konstanz.de; Tel: +49-(0)7531-88-5458*
[b] *Statistical and Computational Physics, Department of Physics, University of Konstanz, Universitaetsstrasse 10, D-78464 Konstanz, Germany. E-mail: peter.nielaba@uni-konstanz.de*

‡ These authors contributed equally to this work.

particle diffusion[24] and order[25] in different model systems like micro-channels. Examples of the effects observed are single file diffusion,[26] especially in the high density regime, and an influence of the confining walls on the orientational degrees of freedom.[27] By employing a variation of the Brownian dynamics algorithm which was already successfully utilised to model spherocylinders[28,29] and three-dimensional dumbbells,[30] it is possible to foster the understanding of the structure of dumbbell monolayers in direct comparison with experiments.

In this work, the Langmuir–Blodgett method is used to generate closely packed dumbbell monolayers. The resulting overarching structures of the colloid films are explored by electron microscopy and further image analysis. To complement these studies, we approximate the Langmuir–Blodgett method with Brownian dynamics simulations of two-dimensional dumbbells between confining walls. In detail, soft wall boundary conditions with variable positions are used to model the movement of the barriers in the experiments. By reducing the distance between the soft wall boundaries, high density dumbbell monolayers are modelled which can be compared to the colloid assemblies.

A comprehensive comparison between experimental dumbbell particle monolayers and computational data from the Brownian dynamics simulations is made by utilising Voronoi tessellations and the analysis of several key features. Among others, the packing density, pair correlation functions and the Voronoi shape factor are viewed in the light of several confinement parameters, thus deepening the understanding of the assembly of anisotropic particle monolayers.

We find that the order of the monolayers is highly dependent on the final area fraction. Enhancing the density of the assembly leads to a sharper progression of the probability density of the Voronoi shape factor and a growth in the percentage of domains containing particles with six nearest neighbours. Especially for higher area fractions, these domains can consist of dumbbells with side-by-side alignment which induces a local anisotropy in the homogeneous monolayers. In the experiments, a reduction of the barrier speed increases the area fraction for a fixed target surface pressure which results in more ordered monolayers. By varying the interaction strength, the structure of the simulated monolayers can be tweaked. Overall, the simple simulation model and experiments are in excellent qualitative agreement with each other.

This work is structured as follows: first the materials and methods are outlined briefly in Section 2. Here the fundamentals of the experiments and the Brownian dynamics simulations are described. Furthermore, a preliminary discussion which compares the experimental set-up and the conducted simulations in detail is presented. This section is concluded with an exposition of the quantities analysed in this work. The main findings and results are discussed in Section 3. After a short qualitative discussion of the monolayers and the corresponding Voronoi tessellations, the influence of parameters like the final area fraction, the barrier speed and the interaction strength on the structure of the monolayers is presented. Moreover, the particle alignment is discussed in more detailed. Finally, a summary and an outlook in Section 4 outline the main findings and the steps for further research.

2 Materials and methods

A direct comparison of experimental results with data gathered using Brownian dynamics simulations is made. This section will introduce key concepts of the experiments and the simulations alike.

2.1 Materials

Trimethoxysilylpropylacrylate (TMSPA, 98%), potassium persulfate ($\geq$99%), sodium 4-vinylbenzenesulfonate (NaSS, 99%) and azobisisobutyronitrile (AIBN, 98%) were purchased from Sigma-Aldrich and used as received. Styrene (99%, Merck) was passed over a column filled with inhibitor remover (Sigma-Aldrich) before use. Ethanol (99.8%) and sodium dodecylsulfate (SDS, $\geq$99%) were purchased from Carl Roth. Silicon wafers were cut from 150 cm spherical wafers of 675 μm thickness obtained from Active Business Company. Deionised water (resistivity $\geq$18 μΩ cm) obtained from a reverse osmosis water purification system (Millipore Direct 8) was used for all experiments. Spectra/Por7 dialysis membranes with MWCO: 50 kDa were purchased from Spectrum Labs.

2.2 Particle synthesis

The synthesis of dumbbells was carried out in a similar manner to the previously reported procedure by Dufresne *et al.*[8] and consists of three distinct reaction steps: firstly, spherical polystyrene particles were obtained *via* emulsion polymerization. These particles were coated with a hydrophilic shell of a statistical poly-TMSPA-*co*-polystyrene polymer in a subsequent seeded growth polymerization. Lastly, the dumbbell shape was achieved by another seeded growth step in which the interplay between reduced swelling capacity and hydrophilic coating of the core shell particle lead to a protrusion after polymerization.[31]

The first reaction step was performed by dissolving sodium dodecyl sulfate (1.954 g, 6.775 mmol) in deionized water (1279.38 g) in a round bottom flask. Styrene (201.19 g, 1.932 mol) was added to the reaction, which was kept under N_2 atmosphere, and stirred at 250 rpm. The mixture was heated to 80 °C in a water bath and a solution of potassium persulfate (1.920 g, 7.102 mmol) in deionized water (20.03 g) was added once the temperature was reached. After 8 h reaction time, the resulting dispersion was cooled down to room temperature and filtered through glass wool to remove coagulate.

In the second step, the hydrophilic shell was prepared as follows: the core particle dispersion (132.46 g, 13.53 wt%) was diluted with deionised water (144.48 g) in a round bottom flask, kept under N_2 atmosphere, and stirred at 200 rpm. A mixture of styrene (17.35 g, 167 mmol), TMSPA (1.78 g, 7.167 mmol) and AIBN (105.3 mg, 0.641 mmol) was prepared, degassed and added to the reaction mixture. The reaction was heated to 70 °C in an oil bath and kept at the temperature for 8 h. Afterwards the dispersion was cooled to room temperature and filtered through glass wool.

For the synthesis of dumbbell particles the core–shell dispersion (41.35 g, 12.02 wt%) was diluted with a solution of NaSS (35.5 mg, 0.172 mmol) in deionised water (132.7 g). The reaction mixture was kept under N_2 atmosphere, and stirred at 200 rpm. A solution of AIBN (34.3 mg, 0.209 mmol) in styrene (5.43 g, 52.14 mmol) was prepared, degassed and added to the reaction mixture. The flask was heated to 70 °C in an oil bath and kept at this temperature for 8 h. Subsequently the dispersion was cooled to room temperature and filtered through glass wool.

The dispersion was purified *via* dialysis against deionised water. The lobes of the resulting dumbbell particles were almost symmetrical with diameters of 168.2 nm and 171.0 nm respectively. The centre-to-centre distance of the dumbbell lobes was measured as 93.1 nm. All data was obtained from transmission electron micrographs.

2.3 Langmuir–Blodgett assembly

To observe structure formation of close-packed dumbbell particles the Langmuir–Blodgett method was employed. Advantages of this method include a high reproducibility of the results, an easy automation of the process and the ability to coat substrates on the cm scale. Fig. 1 shows a schematic representation of the experimental procedure.

Langmuir–Blodgett assembly of dumbbell particles was carried out on a KSV NIMA trough set-up with a Langmuir balance and dipper. The surface area of the liquid subphase in the trough was 145 mm × 580 mm. A dipping well in the middle of the trough allowed the immersion of a silicon wafer prior to the spreading of the particle dispersion. The experimental set-up is depicted in Fig. S1 of the ESI.† Before spreading the dispersion, the trough was thoroughly cleaned with dish soap, rinsed with water, EtOH and deionised water. The trough was filled with deionised water and each experiment was preceded by sucking up water from the interface while the barriers moved together, thus eliminating any impurities. This was checked in a compression experiment without any particles in which the surface pressure did not exceed 0.3 mN m^{-1}. The temperature for all experiments was set to 25 °C, with a deviation of no more than 1 °C. This leads us to estimate the viscosity of the water phase as 0.89 mPa s and the density as 0.997 g cm^{-1}.

The following sample preparation was applied for all samples: 1.5 ml of dumbbell particle dispersion was mixed with 500 µl of EtOH and treated in an ultrasonic bath for 30 s. The dumbbell particle dispersions were purified before the experiments *via* dialysis to exclude effects of impurities on the structure formation, such as the formation of non-close-packed structures caused by amphiphilic impurities.[32] For all experiments the dispersion was mixed with ethanol to facilitate spreading on the air/water interface. Because ethanol is known to desorb impurities from the particle surface the dispersion-to-ethanol ratio was kept at a high volume ratio of 3 : 1.[32] This also lowers the risk of aggregation of the particles at the interface due to solvent evaporation.[33] Spreading of the resulting dispersion was done *via* a 100 µl pipette. After spreading, the set-up was given 20 min to equilibrate. Silicon wafers of 1 cm × 1 cm were cleaned with a NH_3/H_2O_2/deionised water (1 : 1 : 5) solution, thoroughly rinsed and treated with O_2 plasma for 10 min before each experiment. The surface pressure isotherms recorded during the experiments confirm the absence of amphiphilic impurities. Small droplets of the dispersion/ethanol mixture (about 5 µl each) were carefully placed at the interface with a pipette tip. Although it has been reported that direct placement of the drops can lead to turbulent mixing with the subphase and subsequent loss of material,[34] we found the particles to be sufficiently surface active to form close-packed, non-overlapping monolayers.

The packing density of dumbbell particles at the interface was monitored indirectly by measuring the surface pressure of the system, defined as[35]

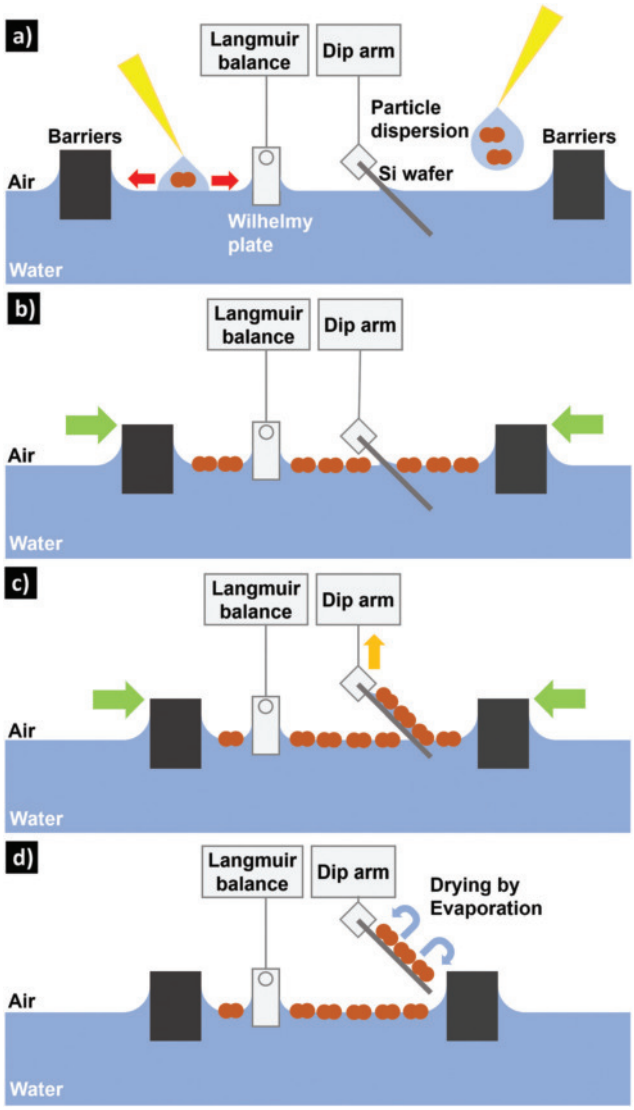

Fig. 1 Scheme of the Langmuir–Blodgett assembly process. (a) Dumbbell-shaped particles dispersed in a water/EtOH mixture (3 : 1) are spread on an air/water interface confined by POM barriers, while the surface pressure is monitored by a Langmuir balance. (b) A dense monolayer of particles is formed at the air/water interface by pushing the barriers together. (c) The monolayer is transferred by lifting the immersed Si wafer while the barriers keep the surface pressure. (d) The monolayer is dried under an angle of 45°.

$$\Pi = \varsigma_0 - \varsigma, \quad (1)$$

where ς_0 is the surface tension of the pure water subphase and ς represents the measured value of the surface tension during the experiment. In total we investigated the structure formation at three different surface pressure values, namely 15, 20 and 30 mN m^{-1}. The speed with which the barriers moved was varied from 0.5 mm min^{-1} to 50 mm min^{-1}. A typical surface pressure isotherm, Π *versus* area per particle, is shown in Fig. S2 of the ESI† for a compression up to a target surface pressure of 20 mN m^{-1}.

After achieving the desired surface pressure, the monolayer was kept at the target for 20 min. The floating monolayer is transferred to a Si wafer that was previously treated with O_2 plasma to maximise wetting and capillary forces depositing the particles on the substrate.[35] Transfer to a silicon wafer was achieved with an attached dip arm under a 45° angle. Afterwards the monolayer was dried under the same angle. We studied the effect of transfer speed in a series of experiments ranging from 0.1 mm min^{-1} to 10 mm min^{-1}. Through the Langmuir–Blodgett method a variety of dumbbell monolayers could be assembled. Fig. 2 shows a selection of micrographs from samples of different final area fractions.

2.4 Drying-mediated assembly

As an alternative assembly method, drying mediated assembly[36] was employed to form particle monolayers. Dispersions of different colloid content were dried overnight on silicon wafers cleaned in the same way as described in the preceding section to enhance wetting. The concentration of the dispersions ranged from 0.1 wt% to 5 wt%. The wafers were dried in a Petri dish with the lid half closed to slow down evaporation and minimise convection effects.[37]

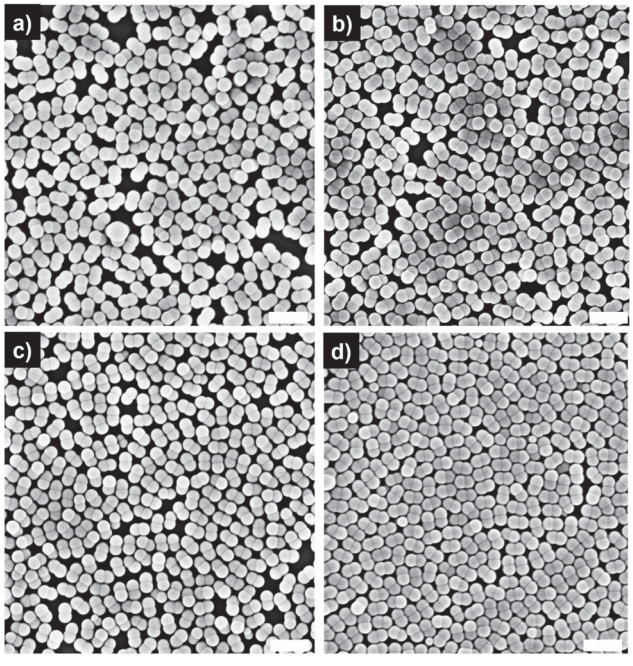

Fig. 2 Monolayers of dumbbell particles at different densities. Images (a–c) show monolayers assembled with the Langmuir–Blodgett method, image (d) shows a film obtained by drying mediated assembly. The target surface pressure and the area fraction ϕ of the Langmuir–Blodgett experiments are (a) 15 mN m^{-1} and 67%. (b) 20 mN m^{-1} and 70%. (c) 30 mN m^{-1} and 76%. (d) Drying mediated assembly, ϕ = 80%, 1 wt%. The scale bars indicate 500 nm.

2.5 Electron microscopy

Field emission scanning electron microscopy (FESEM) images were recorded on a Zeiss CrossBeam 1540 XB microscope operating at 3 kV. A 4 nm platinum layer was applied to the dried samples *via* sputter coating to avoid charging effects during imaging. The magnification was kept constant for all images at ×13 540 to facilitate analysis of the micrographs. The selection of parts of the sample was done in regular line intervals with 10 μm to avoid user selection bias. All images were 8.258 μm × 5.540 μm in size and contained between 700–900 particles, depending on sample density. The micrographs shown in Fig. 2 are examples of the images obtained with FESEM.

2.6 Image analysis

All SEM images were evaluated using the open source programme Fiji.[38] The micrographs were converted into binary images using the thresholding function. The values of the threshold were set to encompass as much of the particles as possible and had to be determined by eye because of the different lighting conditions of each measurement. To avoid artefacts of multiple particles being represented as one species, the watershed algorithm[39] was used to separate the colloids from one another. The analyse particle function gave the orientation angle and the centre of mass coordinates of the particles which could be used for further analysis.

2.7 Brownian dynamics algorithm

In parallel to the experiments, we performed conventional Brownian dynamics simulations of two-dimensional dumbbell-shaped colloids which are confined between two moving walls. The particles are suspended in a liquid and hydrodynamic interactions are neglected. By moving the confining walls closer to each other, the area fraction between the walls is raised comparable with experiments based on the Langmuir–Blodgett method. Perpendicular to the walls, periodic boundary conditions are chosen.

In our simulations, the two-dimensional dumbbell shape is based on two overlapping circles or lobes with an identical diameter σ. These circles possess a rigid centre-to-centre distance l which results in a total length $L = l + \sigma$ of the dumbbell-shaped particles. Combining length and diameter of the particles gives another important parameter to describe the dumbbell shape, namely the aspect ratio $p = L/\sigma$. A sketch of a two-dimensional dumbbell is depicted in Fig. 3. The aspect ratio of the dumbbell particles utilised in the experiments is approximately p = 1.55. This value is kept constant during all simulations.

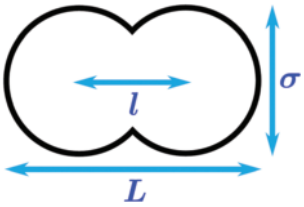

Fig. 3 Sketch of a two-dimensional dumbbell particle. The important parameters are given by the diameter σ, the length L and the centre-to-centre distance l.

The centre positions of the dumbbells $\vec{r}_i$ are updated according to the method introduced for spherocylinders[28,29] and three-dimensional dumbbells.[30] In our simulations however, the corresponding equations of this Brownian dynamics algorithm are modified for two dimensions. Thus, the resulting relations are

$$\vec{r}_i^{\parallel}(t+\Delta t) = \vec{r}_i^{\parallel}(t) + \frac{D^{\parallel}}{k_B T}\vec{F}_i^{\parallel}(t)\Delta t + \sqrt{2D^{\parallel}\Delta t}R_{i,1}\hat{\vec{e}}_i(t), \quad (2)$$

$$\vec{r}_i^{\perp}(t+\Delta t) = \vec{r}_i^{\perp}(t) + \frac{D^{\perp}}{k_B T}\vec{F}_i^{\perp}(t)\Delta t + \sqrt{2D^{\perp}\Delta t}R_{i,2}\hat{\vec{e}}_i^{\perp}(t) \quad (3)$$

for the position components $\vec{r}_i^{\parallel}$ parallel and $\vec{r}_i^{\perp}$ perpendicular to the orientations $\hat{\vec{e}}_i$ of the dumbbells. Here, Δt is the length of the simulation step, T is the temperature and k_B is the Boltzmann constant. The constants $D^{\parallel}$ and $D^{\perp}$ are the diffusion coefficients parallel and perpendicular to the elongated axes of the dumbbells, $\vec{F}_i^{\parallel}$ and $\vec{F}_i^{\perp}$ are the force components parallel and perpendicular to the $\hat{\vec{e}}_i$ and $R_{i,1}$ and $R_{i,2}$ are Gaussian random numbers characterised by vanishing mean $\langle R_{i,1}\rangle = \langle R_{i,2}\rangle = 0$ and the variance $\langle {R_{i,1}}^2\rangle = \langle {R_{i,2}}^2\rangle = 1$. The unit vectors $\hat{\vec{e}}_i^{\perp}$ are generated by

$$\hat{\vec{e}}_i^{\perp}(t) = \left(-e_{i,y}(t), e_{i,x}(t)\right)^T, \quad (4)$$

with $\hat{\vec{e}}_i(t) = \left(e_{i,x}(t), e_{i,y}(t)\right)^T$. In each simulation step, the parallel and perpendicular components of the positions and forces are calculated by

$$\vec{r}_i^{\parallel}(t) = (\hat{\vec{e}}_i(t)\cdot\vec{r}_i(t))\hat{\vec{e}}_i(t), \quad (5)$$

$$\vec{r}_i^{\perp}(t) = \vec{r}_i(t) - \vec{r}_i^{\parallel}(t) \quad (6)$$

and

$$\vec{F}_i^{\parallel}(t) = (\hat{\vec{e}}_i(t)\cdot\vec{F}_i(t)\hat{\vec{e}}_i(t), \quad (7)$$

$$\vec{F}_i^{\perp}(t) = \vec{F}_i(t) - \vec{F}_i^{\parallel}(t) \quad (8)$$

The orientations of the dumbbells have to be updated as well. For this, the equation

$$\hat{\vec{e}}_i(t+\Delta t) = \hat{\vec{e}}_i(t) + \frac{D^{r}}{k_B T}M_i(t)\hat{\vec{e}}_i^{\perp}(t)\Delta t + \sqrt{2D^{r}\Delta t}R_{i,3}\hat{\vec{e}}_i^{\perp}(t) \quad (9)$$

is used, where M_i are the torques acting on the dumbbells, D^r is the diffusion constant of the rotation and $R_{i,3}$ are Gaussian random numbers with the same properties as $R_{i,1}$ and $R_{i,2}$. To maintain the length $|\hat{\vec{e}}_i| = 1$ of the orientation vectors, the $\hat{\vec{e}}_i$ have to be renormalised after each simulation step.

The microscopic diffusion constants $D^{\parallel}$, $D^{\perp}$ and D^r used in the simulations are calculated similarly to previous works[30,40] with the HYDRO++ programme[41–43] and a bead-shell model. For more information regarding the theoretical framework we refer to the numerous works[42,44,45] which discuss the methods used by the HYDRO++ programme in detail. In the calculations following the bead-shell method, the surface of the dumbbell is represented by small beads acting as friction elements. These beads interact with the surrounding liquid *via* friction and with each other *via* hydrodynamic interactions. No-slip boundary conditions are assumed and the hydrodynamic interactions between the beads are approximated up to the third order.[46] With this method, it is possible to calculate the diffusion coefficients for various shells with different numbers and diameters of beads.[40] Afterwards, an extrapolation to the limit of infinite beads with zero diameter can be performed using these results. This extrapolation is utilised to model the microscopic diffusion of the particles. For dumbbells with p = 1.55, the resulting values are $D^{\parallel} = 0.85D^s$, $D^{\perp} = 0.78D^s$ and $D^r = 1.34D^s/\sigma^2$, where D^s is the diffusion coefficient of a sphere with diameter σ.

In the simulations, the interactions between the dumbbells are realised by evaluating the interactions of corresponding lobes pairwise. Thus, if two dumbbells i and j interact, the total force on particle i is given by the sum of the forces acting on its lobes due to the lobes of particle j. The pair potential V between two particular lobes k and l of two dumbbells i and j at the lobe centre positions $\vec{r}_{i,k}$ and $\vec{r}_{j,l}$ is chosen to be

$$V\left(|\vec{r}_{j,l} - \vec{r}_{i,k}|\right) = \Phi_{\sigma/b}\left(|\vec{r}_{j,l} - \vec{r}_{i,k}|\right) \quad (10)$$

with

$$\Phi_a(r) = \begin{cases} 4\varepsilon\left[\left(\frac{a}{r}\right)^{12} - \left(\frac{a}{r}\right)^{6}\right] + \varepsilon, & r \le 2^{1/6}a \\ 0, & r > 2^{1/6}a \end{cases} \quad (11)$$

and

$$b = \int_0^{2^{1/6}} \left[1 - \exp\left(-\frac{\Phi_1(r)}{k_B T}\right)\right] \mathrm{d}r. \quad (12)$$

Here, Φ_a is the conventional Weeks–Chandler–Andersen potential[47] with size parameter a and interaction strength ε. We define the effective diameter of the dumbbells for low particle densities using the Barker–Henderson diameter[48]

$$\sigma_{\mathrm{eff}} = \int_0^{\infty} \left[1 - \exp\left(-\frac{V(r)}{k_B T}\right)\right] \mathrm{d}r. \quad (13)$$

For dumbbell colloids which interact *via* a conventional Weeks–Chandler–Andersen potential (11), the effective diameter depends on the interaction strength ε. Therefore, for a fixed centre-to-centre distance l, the effective aspect ratio would vary by changing ε. Due to this variation, p would become an inappropriate parameter to compare the experiments to simulations with different ε. By utilising the modified Weeks–Chandler–Andersen potential (10), the effective diameter is independent of the

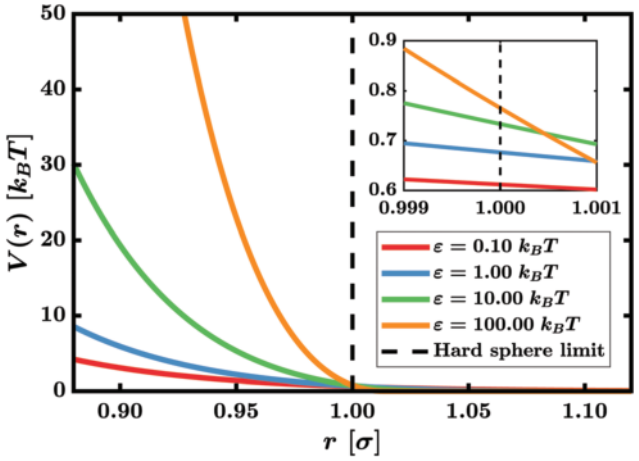

Fig. 4 Modified Weeks–Chandler–Andersen potential for different interaction strengths ε. The inset shows the behaviour near $r = \sigma$ in more detail. The values of ε are given in units of k_BT. The soft edges of the particles become sharper by increasing the interaction strength ε. The axes of the inset are the same as the ones of the whole figure.

interaction strength (and it holds $\sigma_{eff} = \sigma$) for all ε. This can be seen using the transformation theorem on the integration in eqn (13). As a result, the aspect ratio p is identical for dumbbells in (dilute) systems with different interaction strengths and $\sigma_{eff} = \sigma$ is a suitable unit of length.

Fig. 4 shows the progression of the modified Weeks–Chandler–Andersen potential (10) for different interaction strengths ε. By increasing the interaction strength, the soft edges of the particles become overall sharper and the progression becomes significantly steeper.

The interaction between dumbbells also results in torques affecting the orientations of the particles. Let $\vec{F}_{i,k} = (F_{i,k,x}, F_{i,k,y})^T$ be the force which acts on lobe k at lobe centre position $\vec{r}_{i,k}$ of dumbbell i with its centre at $\vec{r}_i$. Furthermore, we define the lever

$$\vec{h}_{i,k} = \vec{r}_{i,k} - \vec{r}_i = \left(h_{i,k,x}, h_{i,k,y}\right)^T \tag{14}$$

with the length $l/2$. The resulting torque $M_{i,k}$ which affects dumbbell i due to $\vec{F}_{i,k}$ is given by

$$M_{i,k} = h_{i,k,x}F_{i,k,y} - h_{i,k,y}F_{i,k,x}. \tag{15}$$

The moving walls are realised by two soft walls similar to the ones in an earlier publication.[27] They move closer to each other with a constant velocity v. During the simulations, the walls are moved in every discrete simulation step after the interaction forces are calculated. In detail, the particle interactions are handled first. Then, the particle–wall interactions are calculated. Finally, the walls are moved. The lobes of the dumbbells interact with the soft walls *via* the conventional Weeks–Chandler–Andersen potential (11) with $a = \sigma/2$ and $\varepsilon = 10k_BT$. It is assumed that a soft wall interacts only with the lobe of a dumbbell closest to its current position. During the calculation, the absolute value of the vector parallel to the shortest distance between the lobes of the dumbbells and the walls is applied for the distance r in eqn (11).

The simulations are performed with $\sigma_{eff} = \sigma$ as the unit of length, k_BT as the unit of energy and D^s as the unit for the diffusion coefficients. The time is given in units of the Brownian time $\tau_D = \sigma^2/D^s$ and the length of a simulation step is chosen to be $\Delta t = 10^{-5}\tau_D$. We define the area fraction of the simulated system using the equation

$$\phi = \frac{N\sigma^2}{2A}\left(\pi - \left[\arccos\left(\frac{l}{\sigma}\right) - \frac{l}{\sigma}\sqrt{1 - \left(\frac{l}{\sigma}\right)^2}\right]\right), \tag{16}$$

where A is the current area of the simulation box. All simulations consist of $N = 3500$ dumbbell shaped particles with aspect ratio $p = 1.55$ which are placed randomly in the simulation box with an initial area fraction of $\phi = 5\%$. After the particles are positioned, the system equilibrates for $50\tau_D$ before the walls start moving. In the next step, the soft walls are moved closer to each other with a constant barrier speed of v until the final area fraction is reached. Beforehand, the width of the system was chosen so that the simulation box is quadratic after the final area fraction is set. The fully compressed system equilibrates once more for $1000\tau_D$ until the analysis is started. The interaction strength ε, the barrier speed v and the final area fraction ϕ are the parameters of the simulations which can be varied.

To give a visual representation for the simulation model of the Langmuir–Blodgett method, Movie S1 of the ESI,† depicts the particle compression based on the moving walls in a scaled-down set-up. This video shows a system of $N = 500$ particles which is compressed from $\phi = 40\%$ to $\phi = 90\%$. The walls move with $v = 7.86\sigma/\tau_D$ and $\varepsilon = 1.0k_BT$ is chosen. For simplification purposes, the system does not equilibrate before the walls start to move. The visualisation has been created with VisIt.[49]

2.8 Preliminary discussions: comparison between experiments and simulations

The experimental set-up of the Langmuir–Blodgett method is complex with a large number of different parameters. The simulations performed in this work, on the other hand, are a simple first approximation of this set-up and thus some major differences are present which should be discussed.

Firstly, the interactions between the charged colloids in the experiments are the sum of multiple different forces and effects like van der Waals forces and Coulomb interactions. However, we assume that the particles in the experiments stay in a solely repulsive regime so that the modelling of the interactions by the simple modified Weeks–Chandler–Andersen potential is justified. We aim to analyse phenomena in the colloidal monolayers which only depend on the particle shape. Thus, qualitative similarities should be visible by using a simple repulsive pair potential in our simulation model. In general, the simulated particles are softer compared to their real counter parts.

Secondly, we use microscopic diffusion constants in our simulations which are calculated with a three-dimensional bead-shell model. As a result, the simulated monolayer fits better to colloids which are confined at the interface between two liquids with the same viscosity while the experiments are conducted at the air/water interface. This could lead to a discrepancy in the ratio of the mobility of the colloids and

the barrier speed between the simulations and the experiments. In our analysis, we assume that this discrepancy is negligible for the colloidal structures compared to other simplifications of our model. We further neglect all phenomena specific to colloids at the interface between two dispersion agents[50,51] in the simulations. Consequences of effects like capillary interactions and capillary assembly are therefore not captured in the two-dimensional Brownian dynamics calculations. However, such phenomena can influence the structure formation in the experiments.

Another important difference is coupled with the accessible input parameters of the experiments and the simulations. In the experiments, the target surface pressure is used to control the barriers. The final area fraction is the result of the structures which form during the experiment at a given surface pressure. In the simulations, we simply regulate the final area fraction directly. This could lead to differences in the colloidal structures of the final state. Because experimental and simulated data are in good agreement, we make the assumption that the qualitative structure of the colloidal monolayers only depends on the final area fraction and the treatment of the moving walls in the high density limit.

When assembling dumbbell monolayers in experiments an upper limit for the area fraction of about 76% at 30 mN m^{-1} achievable with the Langmuir–Blodgett method was found. Samples prepared at higher surface pressure showed a substantial amount of bilayer content and are therefore not considered in the discussion of the results. In the simulations, an area fraction of 90% can easily be reached. Drying mediated assembly resulted in densely packed multilayers for all dispersions used. These samples are difficult to characterise systematically and the results were therefore discarded with one exception. The drying mediated assembly conducted with a 1 wt% dispersion showed an area of a few micrometers in which the dumbbell particles were packed into a dense monolayer that was denser than all samples assembled with the Langmuir–Blodgett method.

Defects based on dumbbells which are oriented out of the two-dimensional plane can be found in the experimental monolayers. These defects are inevitable in the experiments but are not taken into account by the simulations. There is also a small fraction of non-dumbbell shaped colloids present in the experimental monolayers. They undoubtedly affect the local structure and adjacent Voronoi cells. Because the number of these defects appears reasonably small, we assume that the overall structure of the monolayers stays approximately the same. A small selection of experimental defects can be seen in Fig. S3 of the ESI.†

In the experiments, the compressed monolayers are transferred onto a silicon wafer under a 45° angle for further analysis. Moreover, they are dried under this angle as well which could introduce a density gradient in the monolayers. This step of the experiments is not considered in our simulations. We assume that the small variations in density due to the drying angle are negligible compared to the already high area fraction of the monolayers. Capillary phenomena during the drying can influence the experimental monolayers but are neglected in the simulations.

The experimental set-up used for the assembly of dumbbell monolayers *via* the Langmuir–Blodgett method is not suited to transfer films close to the barriers and thus a detailed analysis of the structure near the confining walls is outside of the scope of our study. The discussion of the results therefore focuses on the structure formation of colloidal dumbbells far from the confining barriers which made the particles pack into dense monolayers. However, in contrast to experiments, simulations permitted some predictions regarding the density profile along the axis perpendicular to the walls. These density profiles are depicted in Fig. S4 of the ESI.†

2.9 Quantities of interest

To characterise and describe the details of the particle monolayers, we use Voronoi tessellations[52] which are formed by using the centre positions of the particular dumbbells. For a given set of particle positions, the Voronoi tessellation assigns to each position a polygon called a Voronoi cell which encloses all points of the two-dimensional plane that are closer to that position than to any other centre. In general, each nearest neighbour of the associated centre defines a side of the Voronoi cell. It is thus possible to count the sides or vertices of the polygon to determine the coordination number. To capture the structure of the monolayers in detail, we use the shape factor ζ of the Voronoi cells[21] which was used in various studies over the years.[53–55] It is defined by

$$\zeta = \frac{C^2}{4\pi S}, \tag{17}$$

where C is the perimeter and S is the area of the corresponding Voronoi cell. For a sphere, the shape factor is $\zeta = 1$ and for other shapes, the shape factor is $\zeta > 1$. More precisely, ζ is a parameter of nonsphericity.[21]

By calculating the shape factor for every Voronoi cell in the Voronoi tessellation of every experimental snapshot or of every final frame of the different simulations, we determine the probability density of the shape factor $p(\zeta)$. In detail, the quantity $p(\zeta)\mathrm{d}\zeta$ corresponds to the probability of finding a Voronoi cell with the shape factor $\zeta \in [\zeta - \mathrm{d}\zeta,\zeta]$. We restrict the analysis of our data to values $\zeta < \zeta_{\max}$ with the maximum shape factor $\zeta_{\max} = 1.5$. Therefore, to be more precise, $p(\zeta)\mathrm{d}\zeta$ is the probability of finding a ζ out of $[0,\zeta_{\max}]$ in the interval $[\zeta - \mathrm{d}\zeta,\zeta]$.

The Voronoi tessellation is also used to calculate the probability distribution p(C.N.) for the coordination number, where we define the number of nearest neighbours of a particular dumbbell by the number of the sides or vertices of the corresponding Voronoi cell. The analysis of the coordination number C.N. is restricted by a maximum value of 11.

To further understand the exact structure of the monolayers, we analyse the probability distribution of ζ resolved in terms of the particular coordination number of the Voronoi cells. This means that the probability density of finding a Voronoi cell with a specific C.N. and a $\zeta \in [\zeta - \mathrm{d}\zeta,\zeta]$ is computed.

Another quantity which is used to describe the correlation of the positions inside the monolayer is the two-dimensional pair correlation function

$$g(r) = \frac{1}{\rho N}\left\langle \sum_{i,j=1;i\neq j}^{N} \delta\left(\vec{r} - \vec{r}_{ij}\right)\right\rangle \qquad (18)$$

of the particle centres, where N is the number of particles, $\rho = N/A$ is the area density of an ideal gas in the area A and $\vec{r}_{ij} = \vec{r}_j - \vec{r}_i$ is the separation vector of particle i and particle j.[56] The brackets $\langle\cdot\rangle$ denotes the canonical average.

The anisotropic geometry of the dumbbell particles is central to the superstructures which form under spatial confinement. The alignment of elongated particles in dense systems induce a local anisotropy in the monolayers. To analyse the particle alignment, we compute the orientational pair correlation functions

$$g_\vartheta(r) = \frac{1}{\rho N g(r)}\left\langle \sum_{i,j=1;i\neq j}^{N} \left(2\cos^2(\vartheta_{ij}) - 1\right)\delta\left(\vec{r} - \vec{r}_{ij}\right)\right\rangle. \qquad (19)$$

Here, ϑ_{ij} is the angle enclosed by the orientation vectors $\hat{\vec{e}}_i$ and $\hat{\vec{e}}_j$ of the dumbbells i and j. The orientational pair correlation function is constructed so that $g_\vartheta(r)$ is positive if two dumbbell at distance r are on average oriented parallel to each other. On the contrary, if two particles at distance r are on average perpendicular to each other, $g_\vartheta(r)$ is negative. An arbitrary orientation results in a vanishing orientational pair correlation function.

The analysis of the experimental data for a given set of parameters is based on the average of approximately 100 snapshots of a single monolayer. These snapshots are therefore taken from the same experiment. To calculate the quantities for the simulated systems, the average of between 350 and 500 different simulations is used. Only the final frame of a simulation is utilised for the calculations.

3 Results

The resulting data of the experiments and the simulations show clear similarities indicating general effects and phenomena in the structure formation of dumbbell monolayers which are independent of the exact realisation of the system.

The following sections discuss the Voronoi tessellations first. Afterwards, a quantitative discussion including a comparison between the experiments and the simulations follows. The results of additional simulations are discussed at suitable points.

3.1 Qualitative analysis of Voronoi tessellations

The SEM micrographs reveal structural similarities as well as differences between the different monolayers assembled under varied conditions by the Langmuir–Blodgett method. A selection of micrographs for the most apparent parameter, the target surface pressure and therefore the resulting density of the transferred film, is shown in Fig. 2. The density of particle films increases with higher target surface pressure, leading to a higher area fraction.

Fig. 5 shows a side-by-side comparison of dumbbell particle monolayers obtained by the Langmuir–Blodgett assembly and a Brownian dynamics simulation and the resulting Voronoi tessellations colour coded after the coordination number of the cells. The gaps between particles often appear more uniform in the simulations while the particles assembled by the Langmuir–Blodgett assembly seem to form small areas of densely packed particles with larger gaps produced by drying effects after transfer. See for example the micrographs in Fig. 2. This effect becomes less severe with increased surface pressure and therefore higher area fractions. The micrograph and the simulation snapshot depicted in Fig. 2 show remarkable similarities.

The most common coordination number for Voronoi cells in all samples is six. Instead of a regular hexagonal packing the Voronoi cells are largely stretched, representing the anisotropic nature of the dumbbell particles. Close packed dumbbells seem to prefer a side-by-side orientation resulting in small, elongated Voronoi cells. Large scale packings of this nature are rare in the obtained SEM micrographs. This points to a large degree of freedom of the particle mobility at the air/water interface.

The second and third most common coordination numbers found were five and seven. The presence of these coordination numbers indicate that instead of showing large crystalline areas, the dumbbell monolayer structure is closer to a glassy state. Because of the relatively closely packed assembly and the geometric limitations of neighbouring particles, coordination numbers lower than five or higher than seven were quite rare and are therefore considered negligible for this comparison.

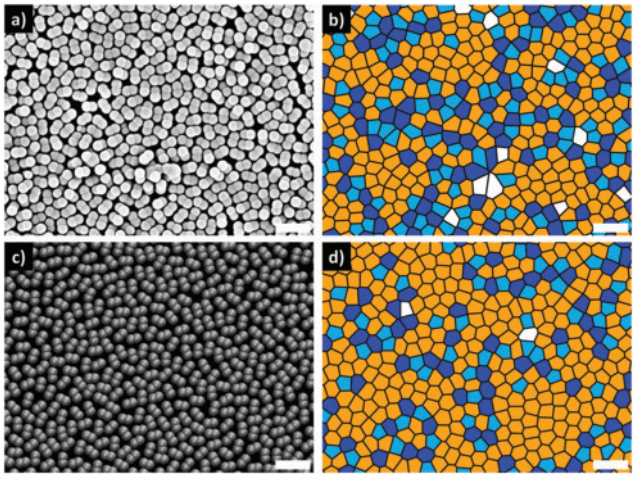

Fig. 5 Comparison of the Voronoi tessellations of dumbbell monolayers assembled by the Langmuir–Blodgett method and Brownian dynamics simulations at similar conditions. (a) SEM micrograph of dumbbell monolayer assembled at 30 mN m^{-1} with a mean area fraction of 76%. (b) Voronoi tessellation of SEM micrograph with a final area fraction of 76%. (c) Visualisation of a Brownian dynamics simulation with a final area fraction of 76%. The visualisation has been created with VMD.[57] (d) The corresponding Voronoi tessellation of the Brownian dynamic simulation with a final area fraction of 76%. The scale bars indicate 500 nm. The Voronoi cells are colour coded to indicate the coordination number. Light blue: C.N. = 5, orange: C.N. = 6, dark blue: C.N. = 7.

While all samples of dumbbells show a relatively close packing, there is some variance between the images taken from the same sample, as well as larger differences between the samples taken at different conditions. Strikingly, the experimental monolayers show a very similar structure to the ones obtained *via* the simulations. Especially the coordination numbers of the Voronoi cells match very well between experiment and simulation. While the transfer speed did not seem to have a significant effect on structure formation of colloidal dumbbells (see Fig. S5 of the ESI†) the parameters of barrier speed and target surface pressure clearly have an impact on the structure of the monolayers. We therefore deem it of considerable interest to look at the quantitative properties of dumbbell monolayers. The next section will describe the results of the parameters used to quantify the differences in the monolayers and compare the experiments to the simulations.

3.2 Quantitative analysis and comparison between experiment and simulation

Using different parameter sets which result in different final area fractions, the resulting Voronoi tessellations vary distinctly. While the corresponding probability densities $p(\zeta)$ are always rather broad which reflects a continuum distribution of ζ, they possess distinguishable features which depend on the varied conditions.

The black curve in Fig. 6 depicts the probability density of the experiments with a barrier speed of 8 mm min^{-1} = 7.86σ/τ_D and a target surface pressure of 30 mN m^{-1} resulting in an average final area fraction of ϕ = 76%. The black dashed line is the corresponding result of the simulations with $\varepsilon = 0.1k_BT$, ϕ = 76% and identical barrier speed. The value $\varepsilon = 0.1k_BT$ is determined by testing multiple interaction strengths and choosing the one whose results agree with the experimental data the best. Experiments and simulations show a shoulder at around ζ = 1.10, a double peak structure between ζ = 1.10 and ζ = 1.25 and a decreasing tail towards larger numbers of ζ. These features are in line with the findings for the well known system of hard discs.[21]

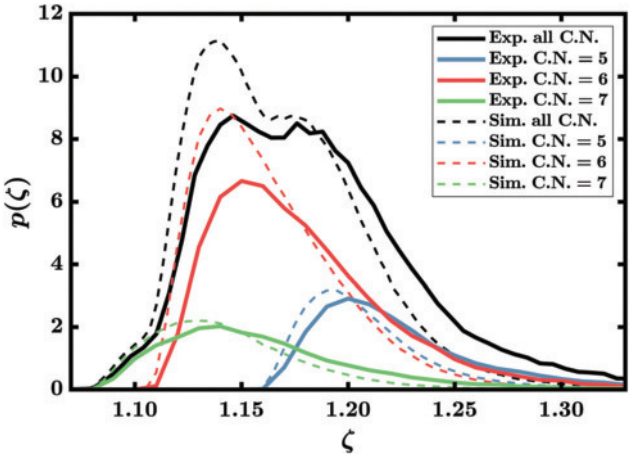

Fig. 6 Probability density $p(\zeta)$ of the shape factor ζ regarding the Voronoi tessellation of a monolayer with area fraction ϕ = 76% for all coordination numbers C.N. and for specific coordination numbers. The dashed curves are the corresponding simulations with an interaction strength of $\varepsilon = 0.1k_BT$. The barrier speed is 7.86σ/τ_D. The visible features of $p(\zeta)$ for all C.N. can be traced back to particles with five, six and seven nearest neighbours.

The behaviour of $p(\zeta)$ can be explained using the probability densities divided up for fixed coordination numbers. The results for experiments and simulations are also depicted in Fig. 6. Comparing the full probability density with the ones with a fixed coordination number, it can be seen that the shoulder at ζ = 1.10 can be traced back to Voronoi cells with C.N. = 7. The first peak of the double peak structure is mostly the result of Voronoi cells with C.N. = 6 with a share of Voronoi cells with C.N. = 7 and the second peak is given by the overlap of the curves with C.N. = 6 and C.N. = 5. The influence of Voronoi cells with other coordination numbers is negligible.

Comparing the results of the experiments with the results of the simulations, it becomes clear that the first peak of the double peak structure is more pronounced in the simulations due to a higher percentage of particles with six nearest neighbours and additionally a sharper progression of the corresponding distribution. Furthermore, the tail towards larger numbers of ζ decreases faster in the simulations. Thus, we conclude that the simulated systems show in general a more ordered overarching structure of the whole monolayer compared to the corresponding experiments. This more ordered state expresses itself by more particles with six nearest neighbours, less defects with five or seven nearest neighbours and sharper distributions of ζ. As visible in Fig. 2 and 5, parallel arrangements of dumbbells are only local in the simulations as well as the experimental assemblies.

3.2.1 Target surface pressure and final area fraction. The target surface pressure and the final area fraction have a major impact on the structure of the monolayer. By enhancing the densities of the monolayers, the distribution of ζ becomes overall sharper and the domains of particles with six nearest neighbours grow.

Fig. 7(a) compares the probability densities $p(\zeta)$ for different target surface pressures and thus for different final area fractions. Depicted are the curves of the target surface pressures of 15 mN m^{-1}, 20 mN m^{-1} and 30 mN m^{-1}. These parameters result in average final area fractions of about ϕ = 67%, ϕ = 70% and ϕ = 76% respectively. The dashed curves in Fig. 7(a) are the corresponding probability densities of the simulations for ϕ = 70% and ϕ = 76%. The barrier speed of the experiments is fixed at v = 8 mm min^{-1} = 7.86σ/τ_D. The same velocity is used in the simulations.

Comparing the probability densities, a clear trend becomes apparent: by increasing the final area fraction, the first peak of the double peak structure which can be traced back to particles with six nearest neighbours becomes more dominant and the tail towards large values of ζ decreases faster. Thus, a higher final area fraction leads to monolayers more dominated by larger structures of particles with coordination number C.N. = 6. As before, we define this as a more ordered state. In general, the simulated systems possess a higher percentage of structures with C.N. = 6 than their experimental counterparts.

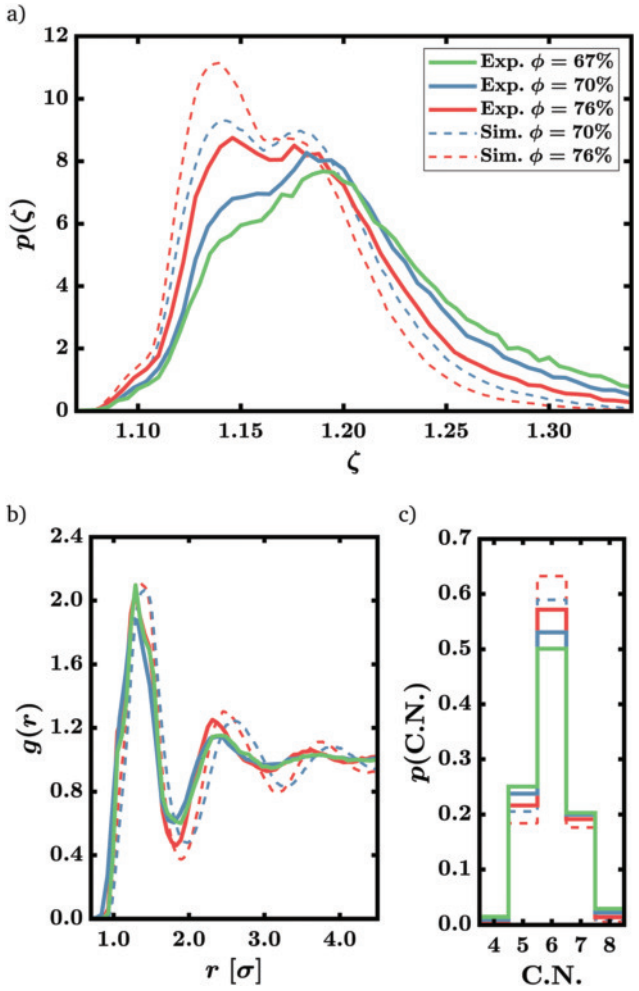

Fig. 7 Quantitative analysis of the monolayer structure for different final area fractions. The dashed curves are the results of the simulations with an interaction strength of $\varepsilon = 0.1k_BT$ which correspond to the experiments. The colours of the curves are matched between the results of the experiments, the corresponding simulations and between the figures (a–c). The barrier speed is $7.86\sigma/\tau_D$. (a) Probability density $p(\zeta)$ of the shape factor ζ for different final area fractions. The first peak becomes more dominant for higher area fractions. (b) Pair correlation functions $g(r)$ for different final area fractions. The differences between the progressions are not as apparent compared to the results of the analysis of $p(\zeta)$. (c) Probability distribution of the coordination number C.N. for different final area fractions. Increasing the final area fractions leads to a higher percentage of particles with six nearest neighbours.

However, we expect that the discrepancies can be minimised by optimising the utilised interaction strength ε in the simulations and by reducing monolayer defects in the real systems.

Fig. 7(b) depicts the pair correlation functions $g(r)$ of the same experiments and simulations. In the first approximation, the resulting curves are quite similar for the analysed experiments. Therefore, we conclude that the probability densities $p(\zeta)$ are better suited to analyse the fine discrepancies between the different dumbbell monolayers. The general progressions of the $g(r)$ curves indicate that, while becoming more structured by increasing the final area fraction, the monolayers are still mostly disordered for the analysed parameter sets. No clear lattice or uniform structure can be found. The pair correlation functions of the experiments possess a sharp substructure in the first peak and the results of the simulations show a more prominent second and third peak in their $g(r)$ progressions. A sharper peak of the experimental data at close distance values suggests harder particles and a denser packing at the local level, while the longer range correlation is not as pronounced as it is in the data from the simulations. This is in line with the observation of higher local area fractions of particles assembled by the Langmuir–Blodgett method compared to the more homogeneous Brownian dynamics simulation. The more homogeneous distribution in simulation data can be attributed to the soft particles of the simulations and the fact that capillary effects between particles on the interface and during drying have not been accounted for in the model.

The corresponding probability distributions of the coordination number are shown in Fig. 7(c). It becomes apparent that the probability of particles with six nearest neighbours is enhanced for systems with a higher final area fraction. In the same manner, the probabilities for Voronoi cells with C.N. = 5 and C.N. = 7 decrease for higher final area fractions. This supports the findings of the analysis of the shape factor probability densities. The simulated monolayers possess a higher percentage of particles with six nearest neighbours. All probability distributions p(C.N.) show an asymmetry with respect to their maximum at C.N. = 6.

The angle distribution of dumbbell particles within monolayers also seems to be slightly less uniform at higher final area fractions. Remarkably, the preference of orientation can be even stronger in the case of dumbbell monolayers obtained from drying mediated assembly, although there is no clear transfer direction in contrast to the Langmuir–Blodgett method. Therefore, we assume that the geometry of the particles itself induces a preferred direction within larger ordered domains. Angle distributions for experimental monolayers of varying area fractions are shown in Fig. S6 (ESI†).

Currently, the parameter range of the experiments is limited by the technical feasibility of sufficiently clear dumbbell monolayers with an insignificant number of bilayer content and defects. These limitations are however irrelevant for simulations. Thus, it is possible to perform further numerical calculations to predict the behaviour of the monolayer outside the range of the experiments.

Using simulations, it is easy to adjust the final area fraction in a broad interval. With this, it is possible to analyse trends which become apparent over drastic changes in the final area fraction. Enhancing the final area fraction leads to a transition from a double peak structure in the progression of $p(\zeta)$ to a single more dominant peak. Furthermore, a substructure is formed in the first peaks of the progression of $g(r)$ and the percentage of particles with six nearest neighbours is increased noticeably the higher the final area fraction rises.

Fig. 8(a) depicts the probability densities of the shape factor ζ for the final area fractions ϕ = 60%, ϕ = 70%, ϕ = 80% and ϕ = 90% and an interaction strength of $\varepsilon = 0.1k_BT$ obtained by simulations. All simulations are conducted with a barrier speed of $v = 7.86\sigma/\tau_D$. Increasing the final area fraction leads to a more

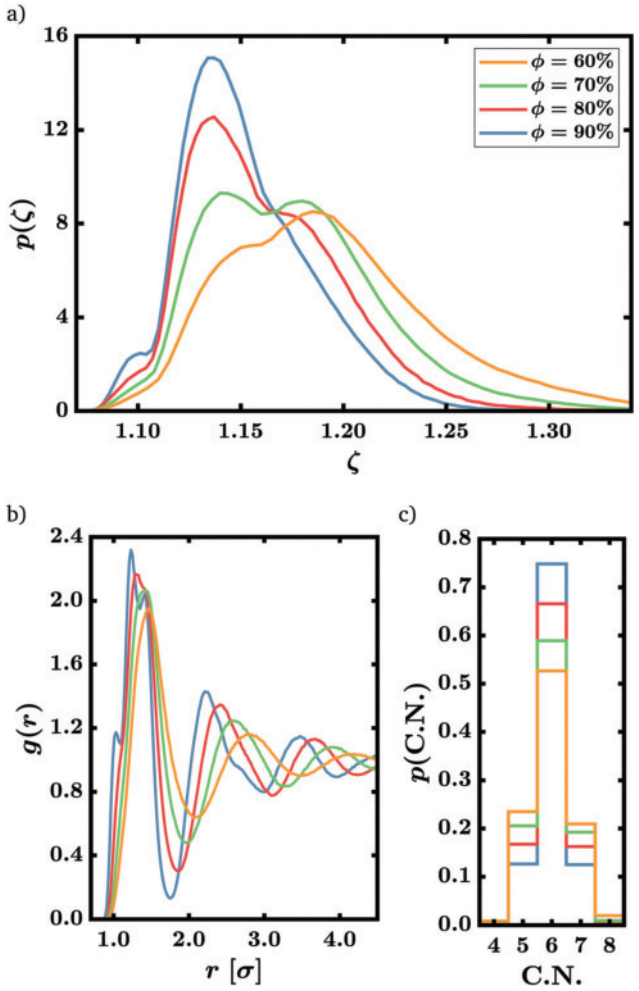

Fig. 8 Quantitative analysis of the monolayer structure for different final area fractions obtained by simulations with interaction strength $\varepsilon = 0.1k_BT$. The colours of the curves are matched between the figures (a–c). The barrier speed is $7.86\sigma/\tau_D$ and the interaction strength is $\varepsilon = 0.1k_BT$. (a) Probability density $p(\zeta)$ of the shape factor ζ for different final area fractions. The first peak becomes more dominant for higher area fractions, while the second peak vanishes. (b) Pair correlation functions $g(r)$ for different final area fractions. A substructure in the first maxima becomes visible in the limit of high area fractions. (c) Probability distribution of the coordination number C.N. for different final area fractions. Increasing the final area fraction leads to a higher percentage of particles with six nearest neighbours.

dominant first peak. Towards higher area fractions, the second peak vanishes while the shoulder at around $\zeta = 1.1$ becomes more pronounced. Altogether, the width of the probability densities is shrinking for higher final area fractions. These results are also represented in the experimental monolayer obtained *via* drying mediated assembly which resulted in a mean area fraction of 80%. Fig. S7(a) of the ESI† shows the sharp peak of the probability density of the coordination number C.N. = 6.

The corresponding pair correlation functions are shown in Fig. 8(b). Small changes of the final area fraction lead to similar pair correlation functions which are nearly identical in the first approximation. However, for larger steps in the final area fractions, changes in the characteristic features of the pair correlation function become noticeable as well. Going from a final area fraction of $\phi = 60\%$ towards a final area fraction of $\phi = 90\%$ the pair correlations function changes from a progression more characteristic for rotationally symmetric or isotropic fluids to a progression with peaks containing complexer substructures for small r. This is typical for a more ordered state at high densities.[21] These findings are again in good agreement with the experimental sample obtained *via* drying mediated assembly and are shown in Fig. S7(b) of the ESI† where a substructure can be seen in the peaks of the pair correlation function.

The probability distributions of the coordination number which correspond to different final area fractions are depicted in Fig. 8(c). The percentage of particles with six nearest neighbours increases for higher final area fractions. This is in agreement with the results depicted in Fig. 8(a). It is noticeable that even for high area fractions like $\phi = 80\%$ and $\phi = 90\%$, the percentages of particles with five and seven nearest neighbours are each higher than 10% and thus stay significant for the overall structure of the simulated monolayers.

The quantitative findings of the simulations can also be seen directly in the corresponding Voronoi tessellations. Fig. 9 depicts examples of Voronoi tessellations of each analysed final area fraction. An enhancement of the final area fraction reflects itself in a higher percentage of particles in more ordered areas or phases with a coordination number of C.N. = 6. Especially for monolayers with high area fractions, the particles with six nearest neighbours are grouped together to clusters or domains with higher local translational order. Some of these areas possess a local orientational order which is indicated by nearly uniform Voronoi cells with an anisotropic shape bordering on each other. An example for such an area is marked with a white circle in Fig. 9. The approximately uniform Voronoi cells represent dumbbells which are parallel to each other. These dumbbells which show a side-by-side orientation are also visible in the experiments as captured in Fig. 2.

3.2.2 Barrier speed. Varying the barrier speed in the experiments leads to different final area fractions despite of a fixed target surface pressure. By decreasing the barrier speed, the order of the monolayers can be enhanced.

Fig. 10(a) depicts the probability densities $p(\zeta)$ of experiments with a fixed target surface pressure of 20 mN m^{-1} and the barrier speeds $v = 0.5$ mm min^{-1} $= 0.49\sigma/\tau_D$, $v = 8$ mm min^{-1} $= 7.86\sigma/\tau_D$ and $v = 50$ mm min^{-1} $= 49.13\sigma/\tau_D$. These barrier speeds give the average final area fractions of approximately $\phi = 72\%$, $\phi = 70\%$ and $\phi = 67\%$. The dashed curves are the corresponding simulations with the same barrier speeds, the same final area fractions ($\phi = 70\%$ and $\phi = 67\%$) and $\varepsilon = 0.1k_BT$.

By decreasing the barrier speed, a higher final area fraction can be achieved with the same target surface pressure. This corresponds to a more dominant first peak in $p(\zeta)$, as seen before. The difference in the probability densities in the experimental monolayers with the same target surface pressure might be explained by capillary forces acting on the particles during the transfer to the silicon wafer. With lower barrier

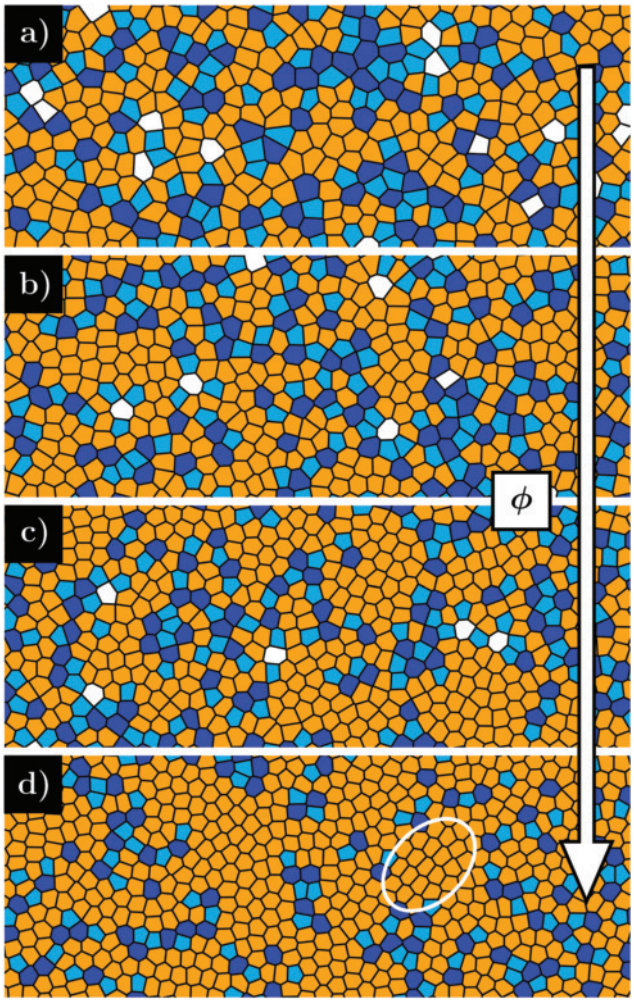

Fig. 9 Voronoi tessellations of simulated dumbbell monolayers for final area fractions of (a) ϕ = 60%, (b) ϕ = 70%, (c) ϕ = 80% and (d) ϕ = 90%. The areas of particles with six nearest neighbours become more pronounced at higher final area fractions. The Voronoi cells are colour coded to indicate the coordination number. Light blue: C.N. = 5, orange: C.N. = 6, dark blue: C.N. = 7. The white circle in (d) marks an area of relatively uniform Voronoi cells with an anisotropic shape. These Voronoi cells indicate a cluster of dumbbells which are parallel to each other. The average distance between the particles is larger for lower area fractions. Thus, the average area of the particular Voronoi cells is shrinking from (a–d).

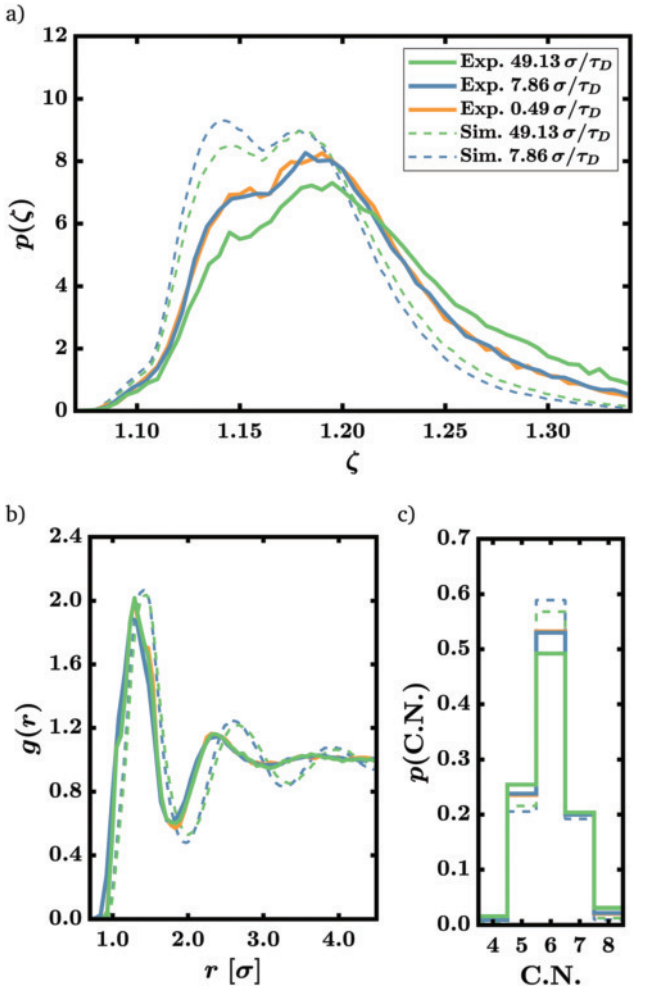

Fig. 10 Quantitative analysis of the monolayer structure for different barrier speeds. The colours of the curves are matched between the results of the experiments, the results of the corresponding simulations and between the figures (a–c). (a) Probability density $p(\zeta)$ for different barrier speeds. The first peak is more dominant for slower moving barriers. (b) Pair correlation functions $g(r)$ for different barrier speeds. The differences between the progressions are not as apparent compared to the results of the analysis of $p(\zeta)$. (c) Probability distribution of the coordination number C.N. for different barrier speeds. Decreasing the barrier speeds leads to a higher percentage of particles with six nearest neighbours.

speeds the particles have more time to orient themselves, thus filling gaps and resulting in a denser packing. Another effect which could explain the lower area fraction for higher barrier speeds are jamming phenomena: due to the higher barrier speeds, the particles are jammed together faster. Therefore, they can not proceed to the expected equilibrium state. While the barrier speed is varied over two orders of magnitude, the differences between the curves in Fig. 10(a) are rather small. Thus, it becomes apparent that the target surface pressure and the final area fraction are more important for tuning the structures of the monolayers.

In Fig. 10(b), the pair correlation functions for the different barrier speeds are shown. While there are clear differences in the probability densities for ζ, the corresponding $g(r)$ curves of the experiments are identical in the first approximation. The general progression indicates a mostly disordered superstructure of the monolayer.

The probability distributions of C.N. in Fig. 10(c) support the findings of the $p(\zeta)$ curves. By decreasing the barrier speed, a higher final area fraction can be reached. These higher final area fractions lead to a higher percentage of particles with six nearest neighbours and thus a higher order.

The results of the simulations provide the same qualitative results and therefore fit to the corresponding experiments. However, the simulated systems possess always a higher percentage of structures or domains with C.N. = 6 and a sharper probability distribution of ζ.

3.2.3 Interaction strength. The simulations are characterised by another parameter given by the interaction strength ε.

Varying this parameter will affect the structure of the monolayers as well. Therefore, simulations are conducted in order to analyse the behaviour for different ε. All simulations are conducted with a barrier speed of $v = 7.86\sigma/\tau_D$ and a final area fraction of $\phi = 70\%$. This area fraction was chosen because it is in the range of the possible densities which can be reached in the experiments based on the Langmuir–Blodgett method.

In systems using the modified Weeks–Chandler–Andersen potential (10), an exponential change of the corresponding interaction strength does not affect the tested model system with $\phi = 70\%$ significantly. An exponential enhancement of the ε leads to slightly more ordered monolayers with a higher percentage of particles with six nearest neighbours and a more dominant first peak.

Fig. 11(a) depicts the probability density of ζ for model systems with interaction strengths of $\varepsilon = 0.1k_BT$, $\varepsilon = 1.0k_BT$, $\varepsilon = 10.0k_BT$ and $\varepsilon = 100.0k_BT$ calculated by simulations. While the interaction strength is raised exponentially, the change in the probability densities is rather marginal. Increasing ε in the modified Weeks–Chandler–Andersen potential of systems with a final area fraction around $\phi = 70\%$ enhances most notably the first peak of the probability density $p(\zeta)$. Systems with higher interaction strengths show the probability density of a more ordered system. However, the difference in $p(\zeta)$ is not significant compared to the change in the probability density if ϕ is varied. Thus, it is possible to tweak the structure of the monolayers based on model systems with the modified Weeks–Chandler–Andersen potential and a final area fraction around $\phi = 70\%$ using the interaction strength, but only small changes in the probability density can be achieved.

The corresponding pair correlation functions are shown in Fig. 11(b). The resulting curves are nearly indistinguishable. However, for higher interaction strengths like $\varepsilon = 10.0k_BT$, a substructure becomes noticeable in the first maximum of the pair correlation function.

An exponential enhancement of the interaction strength in systems with a final area fraction around $\phi = 70\%$ changes the probability distribution of C.N. only slightly. Fig. 11(c) depicts the corresponding distributions. It can be seen that the probability of finding a particle with six nearest neighbours is enhanced for higher ε while the probabilities of finding particles with five or seven nearest neighbours are lowered. However, the differences in p(C.N.) are rather negligible.

Overall, the results of all analysed quantities suggest that the difference between systems with a fixed final area fraction around $\phi = 70\%$ and different ε becomes less severe the higher the interactions strength is.

The influence of the pair potential is in general more prevalent in systems with higher final area fractions. Thus, changes in the interaction strength affects the monolayers more significantly in systems with higher densities. To verify this, we performed additional simulations with a final area fraction of $\phi = 90\%$ and different interaction strengths. The results are shown in Fig. S8 of the ESI.† Increasing the interaction strength from $\varepsilon = 0.1k_BT$ to $\varepsilon = 1.0k_BT$, the first peak of $p(\zeta)$ increases noticeably. The pair correlation function

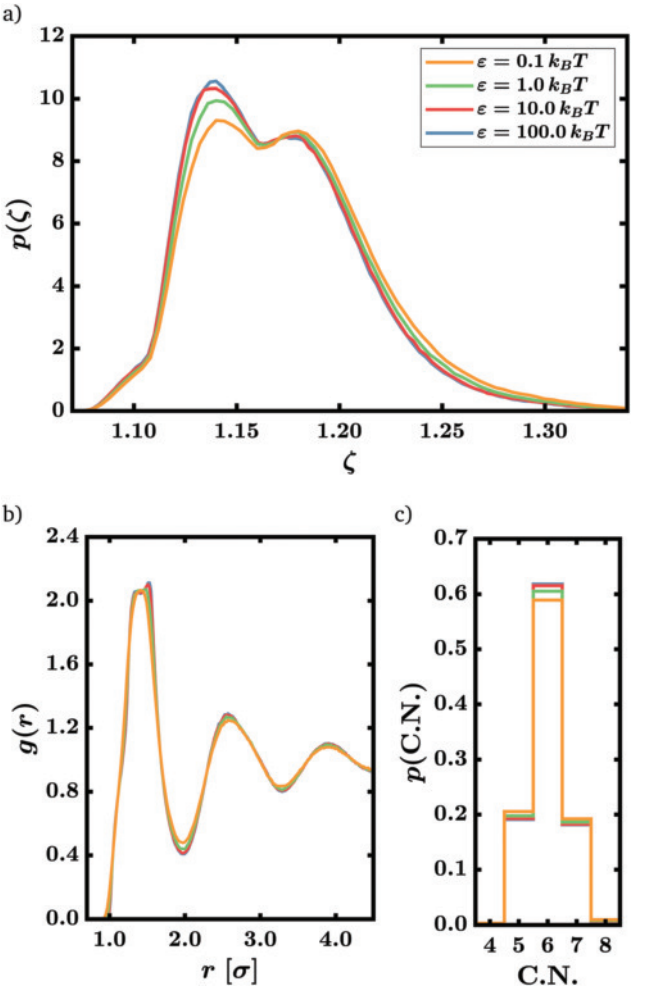

Fig. 11 Quantitative analysis of the model system monolayers with a final area fraction of $\phi = 70\%$ and different interaction strengths ε. The colours of the curves are matched between the figures (a–c). The barrier speed is $7.86\sigma/\tau_D$. (a) Probability density $p(\zeta)$ of the shape factor ζ for different interaction strengths. The first peak becomes more dominant for higher interaction strengths. However, the changes are only small. (b) Pair correlation functions $g(r)$ for different interaction strengths. Changing ε exponentially has nearly no effect. (c) Probability distribution of the coordination number C.N. for different interaction strengths. Increasing ε leads to a higher percentage of particles with six nearest neighbours but the changes are rather small.

develops three distinct peaks for short distances and the probability of finding particles with six nearest neighbours is drastically enhanced. For $\varepsilon = 10.0k_BT$, the system enters a new regime in which the probability density of ζ develops a substructure and therefore additional features. This behaviour confirms that the influence of the interaction strength is more dominant in denser systems. We conclude that changing the interaction strength in simulations at final area fractions in the current density range of the Langmuir–Blodgett experiments tweaks the structure of the monolayer only slightly. However, it can lead to large deviations in dense systems.

It should be mentioned that all statements of this section are specific to the modified Weeks–Chandler–Andersen potential. In models which use other pair potentials like the

conventional Weeks–Chandler–Andersen potential without modifications, we expect the monolayers to express the features of more ordered monolayers to a larger extend if the interaction strength is raised.

In the same manner as presented for the simulations, the structure of real monolayers can be tweaked in systems where the particle interactions are modifiable. Therefore, our results could easily be assigned to real systems in possible future experiments with tunable interactions.

3.3 Particle alignment

Due to the anisotropic nature of the dumbbell colloids, neighbouring particles tend to align. Especially for higher area fractions, larger domains of particles with side-by-side orientation can be found. Fig. 9 shows that these domains of aligned particles are highlighted by the Voronoi tessellations through sections of uniform Voronoi cells. The formation of organized clusters or domains introduces a general but local anisotropy of the monolayer which, for example, distinguishes the monolayers of colloidal dumbbells from those of spherical colloids. To capture this anisotropy, we analyse orientational pair correlation functions $g_\vartheta(r)$ for different final area fractions.

Enhancing the final area fraction influences the magnitude of particle alignment and thus the local anisotropy of the monolayers: For higher area fractions, the orientational pair correlation function develops distinct peaks which indicate the formation of domains of particles aligned parallel to each other.

In Fig. 12(a), the orientational pair correlation functions for the experimental monolayers with average area fractions of ϕ = 67%, ϕ = 70% and ϕ = 76% are depicted. The barrier speed is fixed at $v = 7.86\sigma/\tau_D$ and the corresponding results of the simulations for ϕ = 70% and ϕ = 76% are displayed as dashed lines. The $g_\vartheta(r)$ progressions of the simulations at final area fractions of ϕ = 60%, ϕ = 70%, ϕ = 80% and ϕ = 90% and a barrier speed of $v = 7.86\sigma/\tau_D$ are shown in Fig. 12(b). All simulations are performed with $\varepsilon = 0.1k_BT$. The orientational pair correlation functions are calculated by evaluating the data of every snapshot first and averaging over these results afterwards. At distances where the pair correlation function $g(r)$ vanishes, $g_\vartheta(r)$ is set to zero.

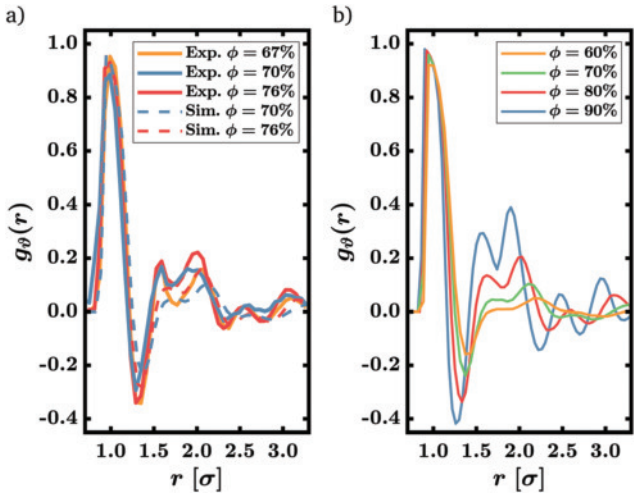

Fig. 12 Orientational pair correlation functions at different area fractions ϕ. The barrier speed is $7.86\sigma/\tau_D$ and all simulations are conducted with $\varepsilon = 0.1k_BT$. (a) The orientational pair correlation functions of experimental dumbbell monolayers are compared with the corresponding simulations. The data of the simulations are displayed as dashed lines. (b) Orientational pair correlation functions of additional simulated systems showing the evolution of the particle alignment over a wide range of final area fractions. The data obtained by experiments and simulations indicate that the double peak structure following the main peak becomes more pronounced for higher final area fractions.

The main peak corresponds to a distance of approximately $r = \sigma$ and results from the anisotropic nature of the dumbbell-shaped colloids: Small distances where neighbouring particles touch each other are only possible if the particles are aligned. Thus, this peak is visible in all $g_\vartheta(r)$ progressions. The most interesting feature of the orientational pair correlation functions is the double peak structure which follows the main peak. The second peak of this structure located at approximately $r = 2.00\sigma$ corresponds to stacks or chains of aligned particles. The first peak of the structure at a distance of about $r = 1.55\sigma$ which is equals to the length of the particles L, is associated with multiple layers of these stacks or chains.

The results of the experiments as well as the simulations indicate that these two peaks become more pronounced at higher final area fractions. This emphasizes the formation of domains of particles aligned parallel to each other with increasing density. Thus, the local orientational order and the overall anisotropy of the monolayers is increased in denser systems. For systems with high area fractions such as the simulated monolayers with ϕ = 90%, even more peaks at higher distances become apparent which is characteristic for a higher state of local orientational order.

While the general $g_\vartheta(r)$ progressions of the experiments and the simulations are in remarkable agreement, the double peak structure of the experiments is more distinct compared to the simulated counterparts at the same final area fraction. This is in line with the qualitative finding of a locally denser packing of the experimental monolayers resulting from capillary forces during the formation and the drying of the nanoparticle films.

4 Conclusions

A detailed comparison between dumbbell assemblies generated with the Langmuir–Blodgett method and a simple (first approximation) simulation model was achieved. Defining a more ordered state by the percentage of particles with six nearest neighbours, a longer range pair correlation and a sharper progression of the shape factor probability density $p(\zeta)$, the simulations result in slightly more ordered systems compared to the experiments with equivalent parameters. Locally, the experimental monolayers often appear to have more densely packed dumbbells while the superstructures predicted by simulations generally seem to be more homogeneous. However, the general agreement between experiments and simulations is remarkable. The simulations show the same

qualitative behaviour and trends as the assembled dumbbell monolayers.

To analyse small changes in the monolayers, the probability density $p(\zeta)$ of the shape factor ζ proved to be appropriate. The general progression of $p(\zeta)$ possesses clear characteristics given by a shoulder for small ζ which corresponds to particles with seven nearest neighbours, a double peak structure and a decreasing tail towards larger values of ζ. The first peak of the double peak structure corresponds mostly to particles with six nearest neighbours and the second peak is a result of particles with five and six nearest neighbours.

Increasing the final area fraction has the strongest effect on the structure of the monolayer: the first peak becomes more dominant for higher final area fractions and the overall progression of $p(\zeta)$ becomes sharper. While small changes of the final area fraction around $\phi = 70\%$ are not visible in the pair correlation function, more drastic changes in ϕ affect the progression of $g(r)$. In the high area fraction limit, the pair correlation function shows a substructure in the first and second maximum. This was shown using additional simulations. Increasing the final area fraction leads to a higher percentage of particles with six nearest neighbours.

In experiments, a variation in the barrier speed v leads to different final area fractions for the same target surface pressure: decreasing the velocity of the barriers increases the final area fraction. Thus, a smaller barrier speed enhances the ability to generate more ordered monolayers with more particles with six nearest neighbours. However, only drastic changes in the barrier speeds influence the overall structure noticeably.

For our simulated model system, we used a modified Weeks–Chandler–Andersen potential with the interaction strength ε. This interaction strength is an additional parameter which can be varied in the simulations. It shows that exponentially increasing the interaction strength of the modified Weeks–Chandler–Andersen potential influences the structure of the monolayers only slightly in systems with an final area fraction around ϕ = 70%. The overall structure can be tweaked with the interaction strength, but the change in order is marginal. It should be mentioned that this statement is specific for the modified version of the Weeks–Chandler–Andersen potential. Other pair potentials could produce different results.

Due to the elongation of the dumbbells, close particles tend to align which leads to a side-by-side orientation in the domains of particles with six nearest neighbours, especially for high area fractions ϕ. These areas of parallel particles appear in the Voronoi tessellations as accumulations of uniform cells. To give a more quantitative description of the particle alignment, we calculated the orientational pair correlation function $g_\vartheta(r)$ for different ϕ. By enhancing the final area fraction, particle alignments expressed as multiple layers of stacks or chains becomes more pronounced. This is indicated by the growth of the $g_\vartheta(r)$ peaks corresponding to the distances $r = 1.55\sigma$ and $r = 2.00\sigma$. For systems with high area fractions, the orientational pair correlation functions develop additional peaks at even larger distances which is characteristic for a state with an enhanced local orientational order.

In this study, we restricted ourselves to a first, general study of the overall structure and order of the monolayers using the Voronoi shape factor ζ, the pair correlation function, an analysis of the coordination number and the orientational pair correlation function. While all investigated quantities provide interesting information regarding the overarching order and structure of the monolayers, the Voronoi tessellation and the corresponding shape factor appear to be most advantageous: Small variations in the monolayers can be easily spotted by comparing the probability densities $p(\zeta)$ and every prominent peak or shoulder of the $p(\zeta)$ progressions can unambiguously be assigned to particles with specific coordination numbers. Even areas of enhanced orientational order are visible in the Voronoi tessellations through uniform cells.

Nevertheless, we are sure that further investigations using other well established order parameters and structure defining quantities can foster the understanding of the overall structure of the monolayers. This could especially benefit the field of new materials with novel properties. For example, the areas of locally aligned dumbbells represented by the uniform Voronoi cells visible in the limit of high area fractions indicate interesting correlation phenomena of the orientational degree of freedom. Using the orientational pair correlation functions, we performed a first quantitative analysis of the degree of particle alignment. However, a detailed study of the domains by establishing distinct cluster affiliation rules and by analysing the corresponding distribution functions could be of particular interest.

Each specific set of cluster affiliation rules emphasises different aspects of the dumbbell monolayers. Therefore, the corresponding cluster distribution functions require a separate study. For example, a cluster could be defined as an ensemble of particles with connecting Voronoi cells which are approximately parallel to the mean orientation of its neighbours. This definition returns primarily small structures based on uniform Voronoi cells. It should be mentioned that there is a finite probability that random arrangements of particles could fulfil such an affiliation rule. Another possibility could be to define a cluster as an ensemble of connected particles which are approximately parallel to at least one of their neighbours which also belong to the cluster. This rule causes larger structures or chains to be identified as clusters, whereas contiguous domains could be split into different smaller clusters. This can happen if the particles in a domain are aligned parallel to the mean orientation of the whole cluster but not perfectly parallel to their direct Voronoi neighbours. To find which definition of a cluster is best suited to describe dumbbell assemblies, detailed studies outside the scope of this article are necessary.

The excellent agreement of experimental assembly and Brownian dynamics simulations shows a complementary way of characterising colloid monolayers. The results of the comparison indicates that our simple Brownian dynamics model is suitable to approximate experiments based on the Langmuir–Blodgett method. Thus, numerous studies with different particle shapes and even colloid mixtures are imaginable. For example, because of the robust nature of the

Brownian dynamics simulations, we are confident in expanding the comparisons between experiments and simulations to monolayers of binary anisotropic particle mixtures. Moreover, the presented analysis could be extended to asymmetric dumbbells with lobes which permit different interactions or are different in size. A particular rich phase behaviour is to be expected in such systems.

Conflicts of interest

There are no conflicts to declare.

Acknowledgements

Financial support from the Deutsche Forschungsgemeinschaft (DFG) within SFB1214/B4 is gratefully acknowledged. Special acknowledgement is given to the technical support from the Particle Analysis Centre (PAC) and the Nanostructure Laboratory (nano.lab) at the University of Konstanz. The authors acknowledge with appreciation the Gauss Centre for Supercomputing e.V. (www.gauss-centre.eu) for funding this project by providing computing time through the John von Neumann Institute for Computing (NIC) on the GCS Supercomputer JUWELS at Jülich Supercomputing Centre (JSC).

References

1 X. Huang, J. Zhou, M. Fu, B. Li, Y. Wang, Q. Zhao, Z. Yang, Q. Xie and L. Li, *Langmuir*, 2007, **23**, 8695–8698.
2 N. Vogel, L. de Viguerie, U. Jonas, C. K. Weiss and K. Landfester, *Adv. Funct. Mater.*, 2011, **21**, 3064–3073.
3 M. Pauly, B. P. Pichon, P. Panissod, S. Fleutot, P. Rodriguez, M. Drillon and S. Begin-Colin, *J. Mater. Chem.*, 2012, **22**, 6343–6350.
4 P. Yang and F. Kim, *ChemPhysChem*, 2002, **3**, 503–506.
5 M. G. Basavaraj, G. G. Fuller, J. Fransaer and J. Vermant, *Langmuir*, 2006, **22**, 6605–6612.
6 S. Acharya, J. P. Hill and K. Ariga, *Adv. Mater.*, 2009, **21**, 2959–2981.
7 Q. Zheng, W. H. Ip, X. Lin, N. Yousefi, K. K. Yeung, Z. Li and J.-K. Kim, *ACS Nano*, 2011, **5**, 6039–6051.
8 J.-G. Park, J. D. Forster and E. R. Dufresne, *J. Am. Chem. Soc.*, 2010, **132**, 5960–5961.
9 J. D. Forster, J.-G. Park, M. Mittal, H. Noh, C. F. Schreck, C. S. OHern, H. Cao, E. M. Furst and E. R. Dufresne, *ACS Nano*, 2011, **5**, 6695–6700.
10 D. Nagao, M. Sugimoto, A. Okada, H. Ishii, M. Konno, A. Imhof and A. van Blaaderen, *Langmuir*, 2012, **28**, 6546–6550.
11 A. F. Demirörs, P. M. Johnson, C. M. van Kats, A. van Blaaderen and A. Imhof, *Langmuir*, 2010, **26**, 14466–14471.
12 M. M. Panczyk, J.-G. Park, N. J. Wagner and E. M. Furst, *Langmuir*, 2013, **29**, 75–81.
13 D. Zerrouki, J. Baudry, D. Pine, P. Chaikin and J. Bibette, *Nature*, 2008, **455**, 380–382.
14 A. C. Newton, T. A. Nguyen, S. J. Veen, D. J. Kraft, P. Schall and P. G. Bolhuis, *Soft Matter*, 2017, **13**, 4903–4915.
15 Y. Han, J. Lee, S. Q. Choi, M. C. Choi and M. W. Kim, *Phys. Rev. E: Stat., Nonlinear, Soft Matter Phys.*, 2013, **88**, 042202.
16 C. Vega, E. P. A. Paras and P. A. Monson, The, *J. Chem. Phys.*, 1992, **96**, 9060–9072.
17 G. Avvisati, T. Vissers and M. Dijkstra, The, *J. Chem. Phys.*, 2015, **142**, 084905.
18 U. Siems, C. Kreuter, A. Erbe, N. Schwierz, S. Sengupta, P. Leiderer and P. Nielaba, *Sci. Rep.*, 2012, **2**, 1015.
19 C. Kreuter, U. Siems, P. Henseler, P. Nielaba, P. Leiderer and A. Erbe, *J. Phys.: Condens. Matter*, 2012, **24**, 464120.
20 E. F. Walraven and F. A. M. Leermakers, *Soft Matter*, 2020, **16**, 3740–3745.
21 F. Moučka and I. Nezbeda, *Phys. Rev. Lett.*, 2005, **94**, 040601.
22 M. X. Fernandes and J. G. de la Torre, *Biophys. J.*, 2002, **83**, 3039–3048.
23 Z. Yang, M. Dutt and Y. C. Chiew, *Mater. Res. Express*, 2019, **6**, 075076.
24 U. Siems and P. Nielaba, *Phys. Rev. E: Stat., Nonlinear, Soft Matter Phys.*, 2015, **91**, 022313.
25 B. Heinze, U. Siems and P. Nielaba, *Phys. Rev. E: Stat., Nonlinear, Soft Matter Phys.*, 2015, **92**, 012323.
26 U. Siems and P. Nielaba, *Phys. Rev. E*, 2018, **98**, 032127.
27 A. Lüders, U. Siems and P. Nielaba, *Phys. Rev. E*, 2019, **99**, 022601.
28 H. Löwen, *Phys. Rev. E: Stat. Phys., Plasmas, Fluids, Relat. Interdiscip. Top.*, 1994, **50**, 1232–1242.
29 A. Patti and A. Cuetos, *Phys. Rev. E: Stat., Nonlinear, Soft Matter Phys.*, 2012, **86**, 011403.
30 N. Heptner and J. Dzubiella, *Mol. Phys.*, 2015, **113**, 2523–2530.
31 B. G. van Ravensteijn and W. K. Kegel, *J. Colloid Interface Sci.*, 2017, **490**, 462–477.
32 M. Rey, T. Yu, R. Guenther, K. Bley and N. Vogel, *Langmuir*, 2019, **35**, 95–103.
33 S. Huang, K. Minami, H. Sakaue, S. Shingubara and T. Takahagi, *Langmuir*, 2004, **20**, 2274–2276.
34 H.-L. Nie, X. Dou, Z. Tang, H. D. Jang and J. Huang, *J. Am. Chem. Soc.*, 2015, **137**, 10683–10688.
35 H. Wu, G. Niu, W. Ren, L. Jiang, O. Liang, J. Zhao, Y. Liu and Y.-H. Xie, *Langmuir*, 2020, **36**, 10061–10068.
36 K. N. Al-Milaji and H. Zhao, *J. Phys. Chem. C*, 2019, **123**, 12029–12041.
37 M. Anyfantakis, Z. Geng, M. Morel, S. Rudiuk and D. Baigl, *Langmuir*, 2015, **31**, 4113–4120.
38 J. Schindelin, I. E. F. Arganda-Carreras, M. L. Verena Kaynig, T. Pietzsch, S. Preibisch, C. Rueden, S. Saalfeld, B. Schmid, J.-Y. Tinevez, D. J. White, V. Hartenstein, K. Eliceiri, P. Tomancak and A. Cardona, *Nat. Methods*, 2012, **9**, 676–682.
39 P. Soille and L. M. Vincent, Determining watersheds in digital pictures via flooding simulations, *Visual Communications and Image Processing '90: Fifth in a Series*, ed. M. Kunt, SPIE, Lausanne, 1990, vol. 1360, pp. 240–250.
40 R. Stuckert, C. S. Plüisch and A. Wittemann, *Langmuir*, 2018, **34**, 13339–13351.

41 J. Garcia de la Torre, S. Navarro, M. Lopez Martinez, F. Diaz and J. Lopez Cascales, *Biophys. J.*, 1994, **67**, 530–531.
42 J. Garcia de la Torre, G. del Rio Echenique and A. Ortega, *J. Phys. Chem. B*, 2007, **111**, 955–961.
43 J. Garcia de la Torre and S. Harding, *Biophys. Rev.*, 2013, **5**, 195–206.
44 B. Carrasco and J. Garcia de la Torre, *J. Chem. Phys.*, 1999, **111**, 4817–4826.
45 B. Carrasco and J. G. de la Torre, *Biophys. J.*, 1999, **76**, 3044–3057.
46 M. Hoffmann, C. S. Wagner, L. Harnau and A. Wittemann, *ACS Nano*, 2009, **3**, 3326–3334.
47 J. D. Weeks, D. Chandler and H. C. Andersen, *J. Chem. Phys.*, 1971, **54**, 5237.
48 J. A. Barker and D. Henderson, *J. Chem. Phys.*, 1967, **47**, 4714–4721.
49 H. Childs, E. Brugger, K. Bonnell, J. Meredith, M. Miller, B. Whitlock and N. Max, *VIS 05. IEEE Visualization, 2005*, 2005, pp. 191–198.
50 I. B. Liu, N. Sharifi-Mood and K. J. Stebe, *Annu. Rev. Condens. Matter Phys.*, 2018, **9**, 283–305.
51 C. Anzivino, F. Chang, G. Soligno, R. van Roij, W. K. Kegel and M. Dijkstra, *Soft Matter*, 2019, **15**, 2638–2647.
52 F. Aurenhammer, *ACM Comput. Surv.*, 1991, **23**, 345–405.
53 S. Živković, Z. M. Jakšić, D. Arsenović, L. Budinski-Petković and S. B. Vrhovac, *Acta Phys. Pol., A*, 2011, **120**, 246–251.
54 K. Franzrahe and P. Nielaba, *Phys. Rev. E: Stat., Nonlinear, Soft Matter Phys.*, 2007, **76**, 061503.
55 K. Franzrahe and P. Nielaba, *Phys. Rev. E: Stat., Nonlinear, Soft Matter Phys.*, 2009, **79**, 051505.
56 H. Löwen, *J. Phys.: Condens. Matter*, 1992, **4**, 10105–10116.
57 W. Humphrey, A. Dalke and K. Schulten, *J. Mol. Graphics*, 1996, **14**, 33–38.